



# Loss Assessment of the NASA Source Diagnostic Test Configuration Using URANS With Phase-Lagged Assumption

Maxime Fiore, Majd Daroukh, Marc Montagnac

## ► To cite this version:

Maxime Fiore, Majd Daroukh, Marc Montagnac. Loss Assessment of the NASA Source Diagnostic Test Configuration Using URANS With Phase-Lagged Assumption. *Journal of Turbomachinery*, 2022, 144 (5), 10.1115/1.4052813 . hal-03553037

**HAL Id: hal-03553037**

**<https://hal.science/hal-03553037>**

Submitted on 2 Feb 2022

**HAL** is a multi-disciplinary open access archive for the deposit and dissemination of scientific research documents, whether they are published or not. The documents may come from teaching and research institutions in France or abroad, or from public or private research centers.

L'archive ouverte pluridisciplinaire **HAL**, est destinée au dépôt et à la diffusion de documents scientifiques de niveau recherche, publiés ou non, émanant des établissements d'enseignement et de recherche français ou étrangers, des laboratoires publics ou privés.

# Loss assessment of the NASA SDT configuration using URANS with phase-lagged assumption

**Maxime Fiore**

DAEP, ISAE-Supaero  
Toulouse, France

Email: maxime.fiore@isae-superaero.fr

**Majd Daroukh**

DAAA, ONERA  
Châtillon, France

Email: majd.daroukh@onera.fr

**Marc Montagnac**

CFD team, CERFACS  
Toulouse, France

Email: montagnac@cerfacs.fr

*This paper presents the study of the Source Diagnostic Test fan rig of the NASA Glenn (NASA SDT). Numerical simulations are performed for the three different Outlet Guide Vane (OGV) geometries (baseline, low-count and low-noise) and three rotational speeds corresponding to approach, cut-back and sideline operating conditions respectively. Unsteady Reynolds Averaged Navier-Stokes (URANS) approach is used. The in- and out-duct flow including the nacelle are considered in the numerical simulations and results are compared against available measurements. Due to the blade count of the fan and OGVs (22 fan blades and either 54 or 26 blades for the OGVs), the simulation can only be reduced to half the full annulus simulation domain using periodic boundary conditions that still represents a significant cost. To alleviate this issue, a URANS with phase-lagged assumption is used. This method allows to perform unsteady simulations on multistage turbomachinery configurations including multiple frequency flows with a reduced computational domain composed of one single blade passage for each row. The large data storage required by the phase-lagged approach is handled by a compression method based on a Proper Orthogonal Decomposition (POD) replacing the traditional Fourier Series Decomposition (FSD). This compression method improves the signal spectral content especially at high frequency. Based on the numerical simulations, the flow field is described and used to assess the losses generated in the turbofan architecture based on an entropy approach. The results show different flow topologies for the fan depending on the rotational speed with a leading edge shock at high rotational speed. The fan boundary layer contributes strongly to losses with the majority of the losses being generated close to the leading edge.*

## 1 Introduction

Upcoming turbofan architectures known as Ultra-High Bypass Ratio (UHBR) turbofans are oriented towards higher bypass ratio for performance purposes. The analysis of the flow field in these kind of configurations is nowadays widely

performed with numerical simulation. These architectures, with wide and highly twisted fan blades and a reduced gap with Outlet Guide Vanes (OGVs), induce a rich flow topology that is challenging to describe. A common test case used for code/numerical validation in propulsive configuration is the NASA Source Diagnostic Test (SDT), which was conducted at the NASA John H. Glenn Research Center in 1999-2000. This configuration offers a rich experimental database including hot wire measurements [1] and laser Doppler velocimetry [2] in the internal channel for aerodynamics and acoustic duct power levels measured using a rotating rake [3]. Recently, this configuration has been simulated based on the full annulus configuration for acoustic characterization. Shur et al. [4] completed a simulation based on Unsteady Reynolds Averaged Navier-Stokes (URANS) approach for the flow upstream of the fan and Improved Delayed Detached-Eddy (IDDES) approach in the interstage, OGV, and exhaust regions at approach and sideline operating points for the baseline OGV configuration. The flow in the NASA SDT was also simulated by Casalino et al. [5] using their Lattice-Boltzmann/Very large LES (VLES) approach based on the PowerFLOW code of the EXA company at approach for the three different OGV configurations. The effect of inlet turbulence, fan Leading Edge (LE) tripping on the fan wake were studied and the effect of a liner on the sound radiated was also assessed. These full annulus simulations make possible to account for any inhomogeneity in the configuration.

For the NASA SDT, the blading geometry is perfectly axisymmetric. Based on the blade count for the fan and OGV rows, the use of periodic boundary conditions makes only possible to reduce to half of the full annulus domain and is still a significant computational cost. The phase-lagged approach allows to reduce the simulation domain to a single passage per row, as proposed by Erdos and Alzner [6] and makes the simulation cost to a manageable level where several OGV configurations and operating points can be tested. However, the main challenge with the phase-lagged approach is the storage requirements of flow variables that are outputted at each time step. To overcome these stor-



Fig. 1: NASA SGT model installed in the NASA Glenn Wind Tunnel

age issues, a data compression method based on a Proper Orthogonal Decomposition (POD) [7] is used. POD compression was implemented in the solver used to perform the present URANS simulations with phase-lagged assumption by Mouret et al. [8].

The purpose of this paper is first to validate the methodology based on URANS with phase-lagged assumption and POD data storage. The capability of this approach is assessed by comparing against the experimental data available: performance quantity and velocity profiles downstream of the fan blade. Once validated, this approach is used to describe the flow field and the mechanisms of loss in the NASA SGT configuration for the three different OGV geometries and operating points

The paper is organized as follows: Sec. 2 introduces the configuration and numerical set up; the method proposed to measure the losses generated in the configuration is described in Sec. 3; the comparison of the numerical simulations against experimental data is presented in Sec. 4; the description of the flow field, including pressure distributions around the blade and near-wall flow, is introduced in Sec. 5; the description of the loss mechanisms is conducted in Sec. 6.

## 2 Configuration and numerical methods

The test case used in the study is the NASA/GE SGT conducted at the NASA Glenn Research Center Cleveland, Ohio in 1999-2000. The configuration shown in Fig. 1 represents the bypass stage portion of a medium pressure ratio, high bypass ratio turbofan engine at approximately 1/5 model scale designed conjointly by NASA and General Electric Aircraft Engines. The NASA SGT configuration has been installed and tested experimentally in a 2.8 m × 4.6 m rectangular test section of a continuous flow wind tunnel at atmospheric pressure conditions able to produce velocities up to  $Ma = 0.23$ . The main geometrical features and dimensions are shown in Fig. 2. The rig is a simplification of a real twin-stream turbofan combining a fan with diameter  $D = 0.5572$  m (hub-to-tip ratio equals to 0.305), the OGVs and a flight-type nacelle in an axisymmetric geometry with

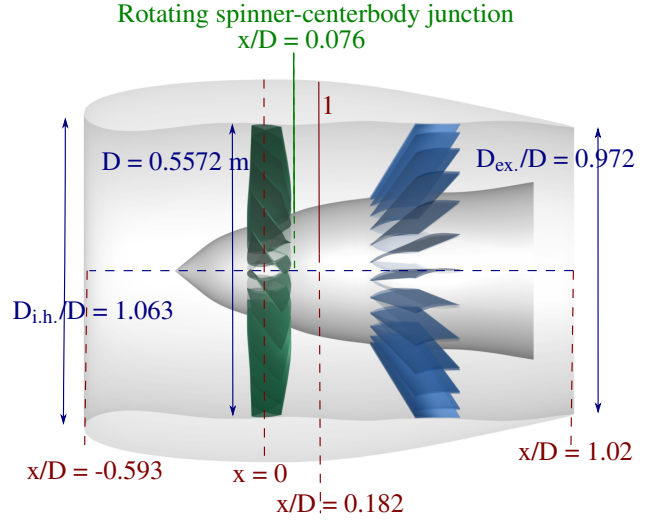


Fig. 2: Main geometrical features and experimental data measurements location (station 1) for the LN OGV configuration

no core flow. The intake highlight diameter is  $D_{i.h.}/D = 1.063$  and the bypass exhaust diameter is  $D_{ex.}/D = 0.972$ . The origin of the reference system used throughout is located in the midpoint of the rotor. The intake lip and bypass exhaust sections are located at  $x/D = -0.593$  and  $x/D = 1.02$  respectively. The location of the junction between the rotating spinner and the centerbody is at  $x/D = 0.076$ . The fan is composed of 22 wide chord blades with a tip clearance of  $h_{tip, clear.}/C_{tip, fan} = 5.4 \times 10^{-3}$  where  $C_{tip, fan}$  is the fan tip true chord at the design point (100% corrected design fan speed). Three different OGV geometries shown in Fig. 3 have been investigated: 54 narrow-chord, high-aspect-ratio vanes representative of a current technology design for this fan pressure ratio (BA); a 26 low-count, wide-chord and low aspect ratio vanes (LC) and a 26 wide-chord, low-aspect-ratio vanes with 30 deg of aft sweep into the vane geometry (LN). Since the purpose of the configuration was to make a fair noise comparison between the three OGV configurations, the total aerodynamic loading for each OGV configuration was kept as equal as possible. This was achieved by keeping the solidity nearly constant (see Tab. 1). This leads to a longer airfoil chord and a larger pitch gap between vanes for the LC and LN configurations compared to BA, keeping the total airfoil area the same for the different OGVs.

The engine operates at zero incidence, the inlet Mach number of the wind tunnel is  $Ma_{\infty} = 0.1$  and the free stream pressure and temperature are  $P_{\infty} = 101,325$  Pa and  $T_{\infty} = 288.15$  K. Three different operating points are considered: Approach (AP), CutBack (CB) and SideLine (SL). Table 2 lists the operating conditions of the rig including the rotational speed at the different operating point as a fraction of the rotational speed at SL.

The simulation domain for the different simulations is shown in Fig. 4. To reproduce the stinger employed in the experiments, a cylindrical prolongation of the center body has been added to the CAD model provided by NASA. The

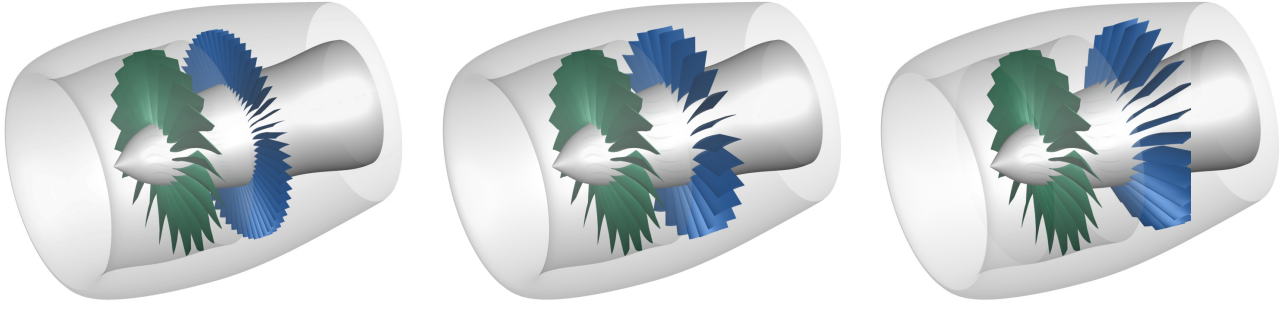


Fig. 3: Geometrical set up features for the three different OGV designs: BA (left), LC (center), LN (right)

Table 1: Geometrical features based on the variants of the OGV configurations: BA, LC and LN OGV setup at pitchline span location

	Fan	BA	LC	LN
No. blades/vanes	22	54	26	26
Stator aft sweep [deg]	-	0	0	30
Aspect ratio $C_x^2/S$	2.00	3.51	1.67	1.67
Solidity $C_x/pitch$	1.73	1.52	1.51	1.53
Stagger [deg]	37.10	10.29	10.68	10.75
Vane camber [deg]	-	34.56	37.57	36.06

Table 2: Nominal conditions during the experimental campaign for different operating points

$P_\infty$ [Pa]	101,325
$T_\infty$ [K]	288.15
Incidence angle [deg]	0
Rotational speed $\omega$ [rad.s <sup>-1</sup> ] (% SL)	AP: 817.6 (61.7%) CB: 1,159.7 (87%) SL: 1,325.4 (100%)
$Ma_\infty$	0.1
$Re_{C_x}$ (SL)	$1.1 \times 10^6$

simulation domain for all the simulations extends 3 D upstream of the LE of the nacelle in the streamwise direction. The outlet is set 8 D downstream of the nacelle Trailing Edge (TE) to recover the free stream conditions and prevent jet reflection effects on the outlet condition. The radius of the simulation domain is 3 D. The simulation domain is split in two sub-domains with different azimuthal extent: a front domain covering 1/22 of the full annulus domain simulating one of the 22 fan blades and a rear domain covering either 1/54 of the full annulus domain (BA) or 1/26 of the full annulus domain (LC, LN) simulating one OGV. For the internal flow, the non-matching interface between the two sub-domains is set between the fan and OGV and on the external domain at the nacelle TE. The boundary conditions imposed at the free surfaces are extrapolation conditions of the reference state

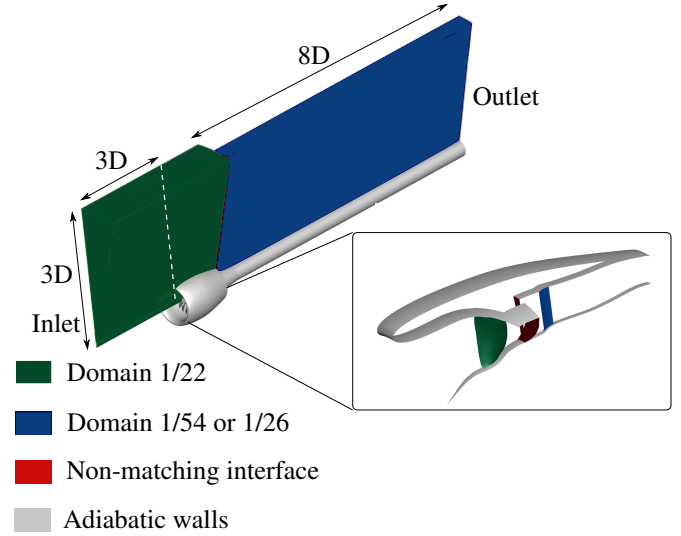


Fig. 4: Simulation domain. Non-matching interface between rotating and static domains. Domain 1/22-1/54 for the BA operating point, 1/22-1/26 for the LC, LN operating points

(see Tab. 2), which is also used as an initial solution for the simulation. Adiabatic, no-slip wall conditions are applied on the fan, OGVs, hub, shroud for the internal domain and on the nacelle wall for the external flow. At the non-matching interfaces between the two sub-domains and on the lateral surfaces, phase-lagged conditions are applied.

The mesh structure is based on an O-6H block for the the fan and OGV rows. Figure 5 shows the mesh around the fan and BA OGV at mid span and in the fan tip gap. The corresponding  $\Delta y^+$  distribution around the fan and OGV for the LN geometry and SL operating point is shown in Fig. 6 with values that remain below unity to meet the requirements for a wall-resolved simulation. The stretching ratio between the size of neighbouring cells in the blade wall-normal direction is set to 1.05. In the streamwise direction, around 300 mesh points are set and 450 in the spanwise direction. The mesh is refined in the wake to properly propagate the structures developing at the TE of the fan and OGVs. In the fan tip gap, 57 points have been set in the spanwise direction. The mesh has been designed to fulfil wall-resolved require-

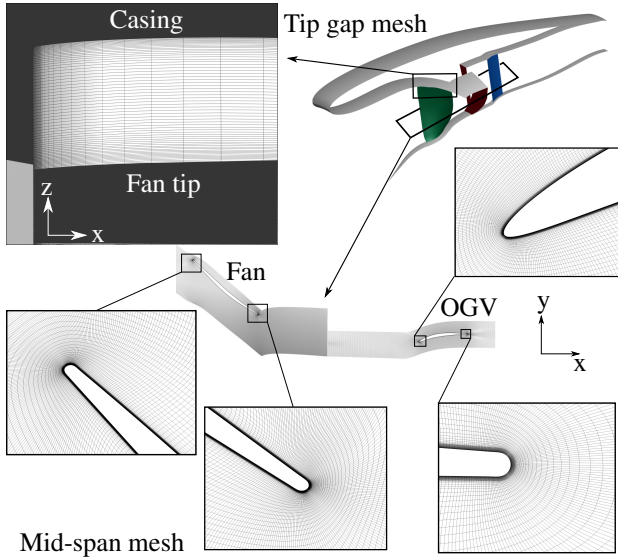


Fig. 5: Mesh around the fan and BASE OGV at midspan and in the fan tip gap

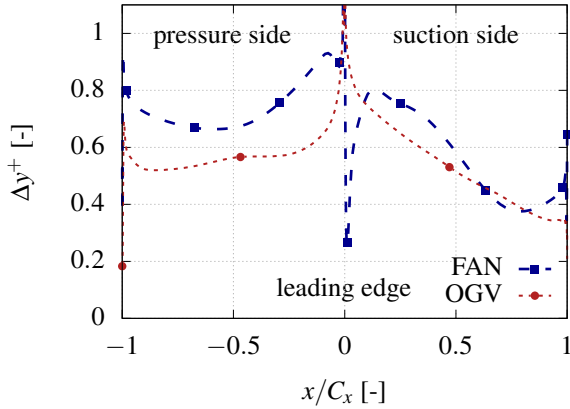


Fig. 6: Grid dimension at the fan and OGV walls for the LN OGV and SL operating point

ments at the spinner, centerbody and the shroud casing walls. The mesh is composed of around  $110 \times 10^6$  cells for the BA,  $120 \times 10^6$  cells for the LC and LN configurations.

The simulations are performed using the ONERA code elsA [9, 10] which solves the compressible Navier-Stokes equations over multi-block structured grids with a cell-centered approach. An upwind Roe scheme with third-order limiter [11] is used for the convective terms. The Wilcox  $k-\omega$  two-equations model with Zheng's limiter [12] is used according to the practice developed by Gourdain [13, 14] in a turbomachinery context for the turbulent transport. Time integration is performed using Dual Time Stepping (DTS) with a Crank-Nicholson scheme (second order accurate) in combination with implicit pseudo-time stepping for the inner loops [15]. The time step is set to  $\Delta t^+ = \Delta t u_\infty / C_x = 3 \times 10^{-4}$  corresponding to 11,880 iterations per full rotation for the BA configuration and 11,440 iterations per full rotation for the LC and LN configurations. The POD compression

method relies on successive singular value decompositions of the matrix composed of the conservative quantities at the phase-lagged interfaces stored dynamically during the simulation. At a given time step, the POD modes from the singular value decomposition are sorted in decreasing energy magnitudes and only the first POD modes are conserved to perform the data compression. For the present study, the 30 most energetic modes are conserved (based on a previous study [8]) and to properly conserve the vortex shedding spectral content generated in the wake of the fan and OGVs at the phase-lagged interfaces. The compressed data stored at the given time step is then imposed later (after a phase-lagged period of time) to the opposite boundary for azimuthal conditions and on the opposed interface for the non-matching interfaces. The storage of azimuthal and non-matching fan-OGV surfaces at each time step for one full rotation in URANS represents a storage requirement of 66.4 GB in POD compared to 217.3 GB for a direct storage. The POD technique used including the update of coefficients gives a CPU overhead of around 34% compared to the spatial and temporal integration in the solver. RANS simulations have been performed to initiate the convergence of the flow field using the same mesh and numerical parameters as the URANS approach except that a pseudo-time integration is used to converge towards a steady state. The non-matching interface is treated with a mixing plane approach and azimuthal conditions with periodic conditions.

The analysis of the flow field detailed in Sec. 5 and 6 is based on a temporally averaged solution of the URANS simulations using 1430 snapshots equally distributed over two full rotations of the configuration. This provides a full three-dimensional solution used to characterize the flow over the different surfaces of the configuration: pressure distribution, friction coefficient and boundary layer quantities based on the boundary layer edge detection method available in elsA [16, 17]. The boundary layer edge detection method is based on a vorticity criterion similarly to the method proposed by Michelassi et al. [18]: for a considered cell surface, the vorticity is calculated in each cell of the cross section following the structured mesh grid. The minimum and maximum value of vorticity denoted  $\Omega_{\min}$  and  $\Omega_{\max}$  over the cross section are stored. When the value :

$$\Omega_{\text{edge}} = \Omega_{\min} + (\Omega_{\max} - \Omega_{\min}) \times 0.01 \quad (1)$$

is reached by a cell of the cross section starting from the cell wall, this mesh point is considered as the edge of the boundary for the considered cell surface point. This procedure is then repeated for any point of the considered surface. The analysis of the flow field is conducted by following the flow through the different components of the NASA SDT configuration for the three different OGV geometries (BA, LC, LN) at the three different operating points (AP, CB and SL). The description of the flow field upstream of the OGVs is made for the LN configuration since the experiments have been led for this configuration and the flow around the different OGV configurations is then described.



Table 3: Summary of LN OGV performance for the different operating points: approach (AP), cutback (CB) and sideline (SL)

Op. point	$\dot{m}$ [kg.s <sup>-1</sup> ]	$\pi^{t-t}$	$\eta$
Experiments			
AP	26.44	1.153	0.857
CB	37.87	1.343	0.865
SL	43.86	1.483	0.872
ADP	45.58	1.488	0.924
RANS			
AP	26.35 (-0.3%)	1.160 (+0.6%)	0.857 (+0.0%)
CB	38.12 (+0.6%)	1.356 (+0.9%)	0.866 (+0.1%)
SL	44.25 (+0.8%)	1.495 (+0.8%)	0.883 (+1.2%)
URANS			
AP	26.40 (-0.2%)	1.159 (+0.5%)	0.863 (+0.7%)
CB	38.05 (+0.5%)	1.360 (+1.2%)	0.87 (+0.5%)
SL	44.05 (+0.4%)	1.50 (+1.1%)	0.882 (+1.1%)

### 3 Measure of loss based on entropy

The increase of entropy in the simulation domain is used to describe the loss generated in the configuration as popularized by Denton in a gas turbine context [19]. In the present study, the entropy generation rate at an axial position  $x$  is calculated by integration of all the cell grid between the station 0 and station  $x$ , the two contributions corresponding to a viscous and a thermal contribution that can be written in (U)RANS formalism:

$$s_{\nabla u}(x) = \iiint_{\mathcal{V}, 0 \rightarrow x} \frac{\tau_{ij, \text{eff}}}{T} \frac{1}{T} \frac{\partial \bar{u}_i}{\partial x_j} d\mathcal{V} \quad (2)$$

$$s_{\nabla T}(x) = \iiint_{\mathcal{V}, 0 \rightarrow x} (\lambda + \lambda_{\text{turb}}) \frac{1}{T^2} \left( \frac{\partial \bar{T}}{\partial x_j} \right)^2 d\mathcal{V} \quad (3)$$

where  $\tau_{ij, \text{eff}} = (\mu + \mu_{\text{turb}})(\partial \bar{u}_i / \partial x_j + \partial \bar{u}_j / \partial x_i)$  is the effective viscous stress tensor,  $u$ ,  $T$  the velocity and temperature field,  $\mu$  and  $\lambda$  the dynamic viscosity and thermal conductivity.  $\bar{\cdot}$  represents the Reynolds averaged quantities as a direct output of the simulation. The different surfaces of the configuration are modelled with adiabatic walls and no temperature inhomogeneity is imposed in the simulation domain leading to a negligible contribution of the thermal term  $s_{\nabla T}$  and a restriction in the analysis to the viscous term  $s_{\nabla u}$ . In a turbulent flow, the viscous entropy term is divided into a mean term (often called the laminar term) and a turbulent term [20]. The former contribution is only due to the mean flow distortion. The latter contribution is induced by turbulence: the mean flow energy at large scale is dissipated at small scales in internal energy (heat) and induces the non-locality between mean energy flow lost and equivalent heat generated at small

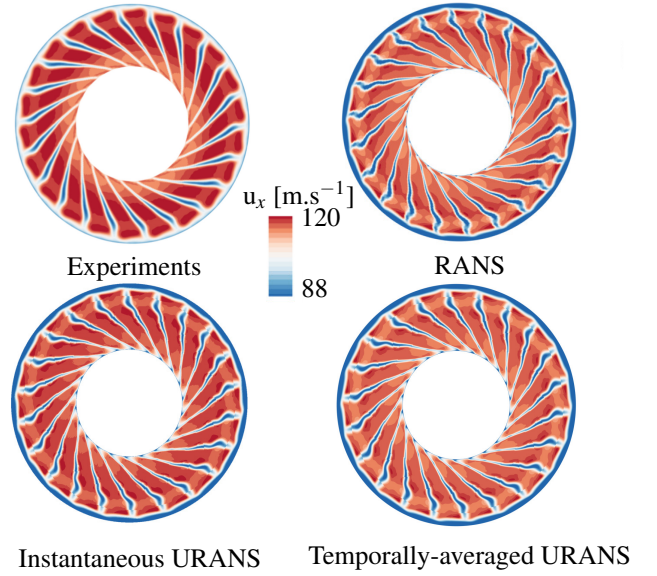


Fig. 7: Comparison of axial velocity at station 1 ( $x = 0.1016$ ) for the experiments, RANS and URANS at AP for the LN configuration

scales. The (U)RANS approach provides a direct splitting between the mean contribution through the natural viscosity of the fluid ( $\mu$ ) and the turbulent contribution with the equivalent turbulent viscosity ( $\mu_{\text{turb}}$ ) [21]. The total contribution is obtained by summing the two contributions as provided in Eq.(2):

$$\begin{bmatrix} s_{\nabla u, \text{mean}} \\ s_{\nabla u, \text{turb}} \end{bmatrix} = \iiint_{\mathcal{V}} \begin{bmatrix} \mu \\ \mu_{\text{turb}} \end{bmatrix} \left( \frac{\partial \bar{u}_i}{\partial x_j} + \frac{\partial \bar{u}_j}{\partial x_i} \right) \frac{1}{T} \frac{\partial \bar{u}_i}{\partial x_j} d\mathcal{V}. \quad (4)$$

## 4 Comparison against experimental data

### 4.1 One dimensional performance quantities

During the experimental test campaign performed in 1999-2000 on the NASA SDT configuration, far-field inlet conditions (denoted  $\infty$ ) consisting of total pressure and total temperature were measured using a floor mounted rake located upstream of the inlet duct. These same quantities were determined downstream of the fan at a station denoted 1 (see Fig. 2) using fixed total pressure/total temperature rakes. Each rake consisted of seven radially-distributed measurement sensors from the center to the shroud casing and each rake was distributed azimuthally [1, 2, 22]. From these measurements were calculated the main flow quantities: the induct mass flow rate  $\dot{m}$ , the total-to-total compression rate of the fan  $\pi^{t-t}$  and the adiabatic efficiency  $\eta$  defined as:

$$\pi^{t-t} = \frac{P_{t,1}}{P_{t,\infty}} \quad \eta = \frac{(\pi^{t-t})^{\frac{\gamma-1}{\gamma}} - 1}{(T_{t,1}/T_{t,\infty}) - 1}. \quad (5)$$

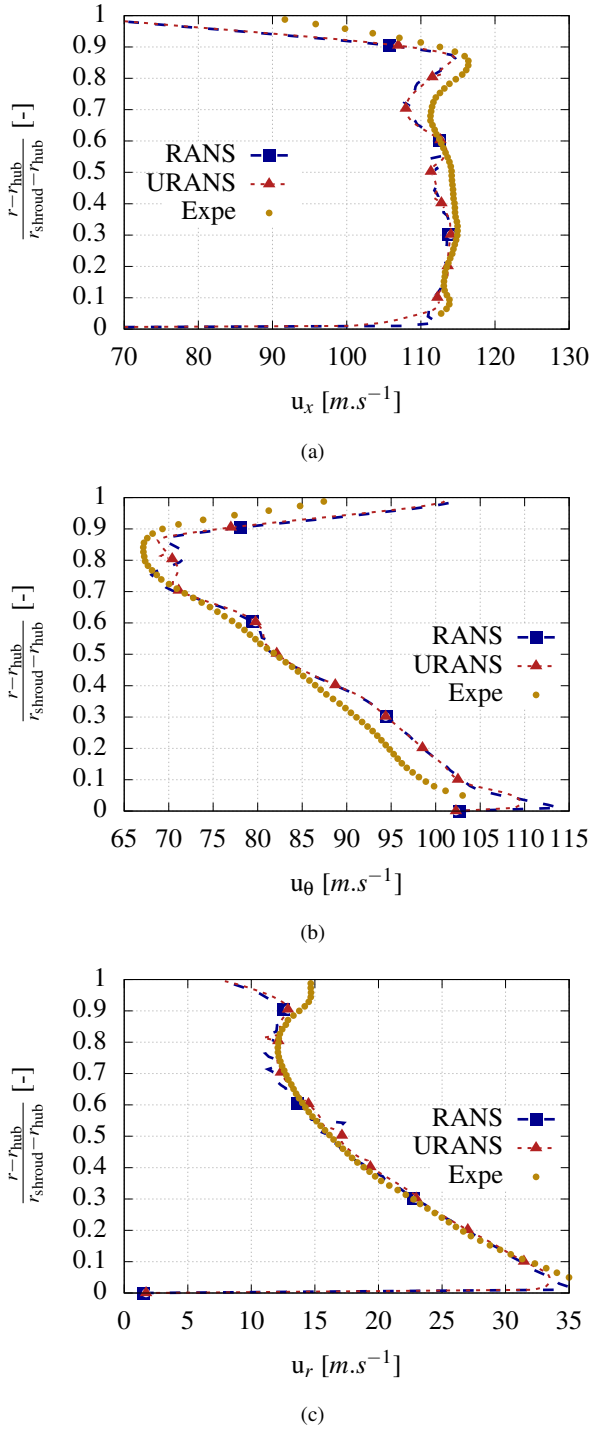


Fig. 8: Comparison of azimuthally averaged axial  $u_x$ , azimuthal  $u_\theta$  and radial  $u_r$  velocity at station 1 for the experiments, RANS and URANS at AP for the LN configuration

The experimental results for the LN OGV configuration at the three different operating points (AP, CB and SL) are compared against the RANS simulations used to initialize the unsteady calculations and URANS with phase-lagged assumption in Tab. 3. In addition, the performances of the engine at the Aerodynamic Design Point (ADP) measured experimentally are provided in same Table. The RANS and URANS

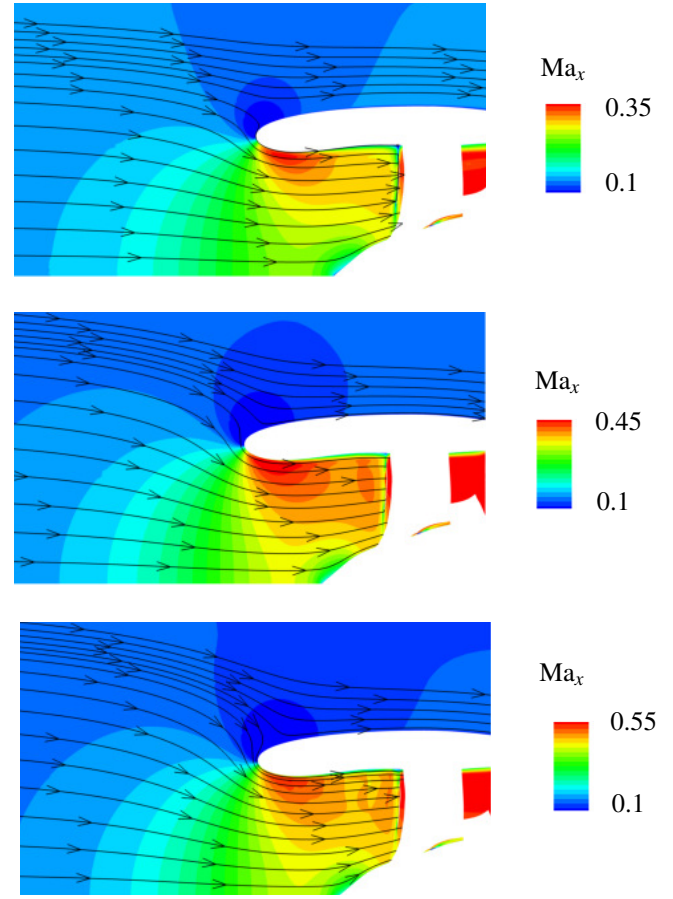


Fig. 9: Axial Mach number and streamlines for the LN configuration at AP (top), CB (middle) and SL (bottom)

simulations are in good agreement with the experiments for the mono-dimensional quantities with a largest discrepancy of around 1.2% with the experiments. The discrepancy increases with the rotational speed but a fair agreement can be observed. The comparison of the performance quantities against experiments for the BA and LC OGVs showed a similar agreement.

#### 4.2 Phase-Locked Velocity Maps

Phase-lock-averaged axial velocity maps  $u_x$  at the station 1 for the different approaches and the LN configuration are shown in Fig. 7. The flow downstream of the fan is composed of regions of low axial velocity corresponding to the fan blade wakes characterized by elongated radially-oriented structures and the tip gap flow close to the casing. The azimuthal averaging of the 2D maps for the axial  $u_x$ , azimuthal  $u_\theta$  and radial  $u_r$  velocity are shown in Fig. 8. The axial, azimuthal and radial velocity profiles obtained with the RANS and URANS show a maximum discrepancy of 5% compared to the experiments, with the largest discrepancy occurring close to the shroud and within the tip gap where all the numerical simulations overpredict the radial velocity break down. The number of points in the tip gap (57 grid points) should be sufficient to properly resolve the tip gap

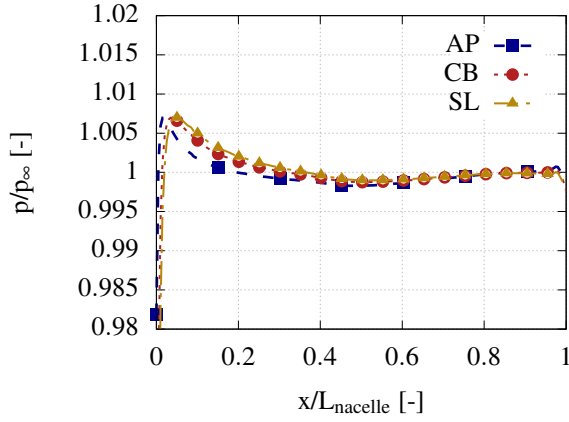


Fig. 10: Azimuthally-averaged static pressure evolution along the nacelle wall for the three different operating points

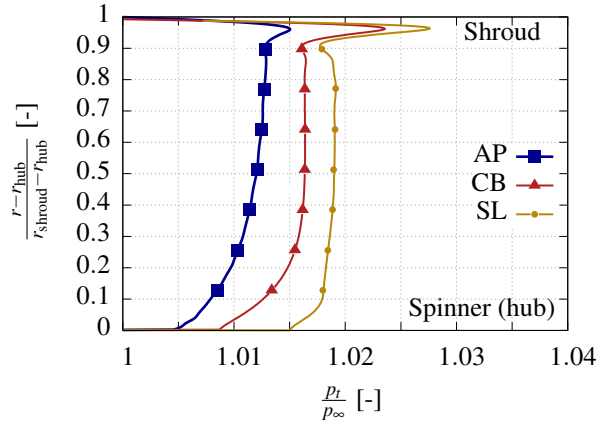


Fig. 12: Radial profiles of inlet total pressure at the beginning of the spinner for the three operating conditions

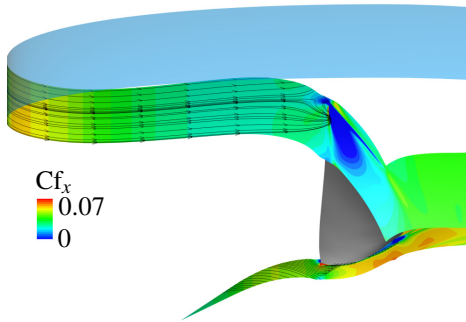


Fig. 11: Axial friction coefficient and streak lines on the hub and shroud surfaces

flow. The prediction inaccuracy may be related to the choice of turbulence model, which fails to reproduce the complex flow physics in the tip gap region and on the upper part of the channel. In particular, a possible improvement would be to use a kL-Smith model that showed its aptitude for better taking into account the compressibility effects [23] than the k- $\epsilon$  or k- $\omega$  used in the present study. Despite this discrepancy, the URANS simulation with phase-lagged assumption matches well the experiments and gives more confidence in its use to describe the flow field and quantify the losses in the configuration.

## 5 Analysis of the flow field

### 5.1 Inlet flow and around the nacelle

Figure 9 shows the axial Mach number and streamlines at the front of the nacelle for the different operating points. The inlet flow at  $Ma = 0.1$  is progressively accelerated by the fan until  $Ma = 0.35$  at AP,  $Ma = 0.45$  at CB and  $Ma = 0.55$  at SL. The upstream stream tube radius increases with the rotational speed corresponding to a captured stream tube area ratio of  $h_{stream\ t.}/D = 1.48$  at AP, 1.82 at CB and 1.96 at SL.

The stagnation point on the nacelle is progressively shifted rearward with the increase of the rotational speed. This behavior can be observed on the pressure distribution around

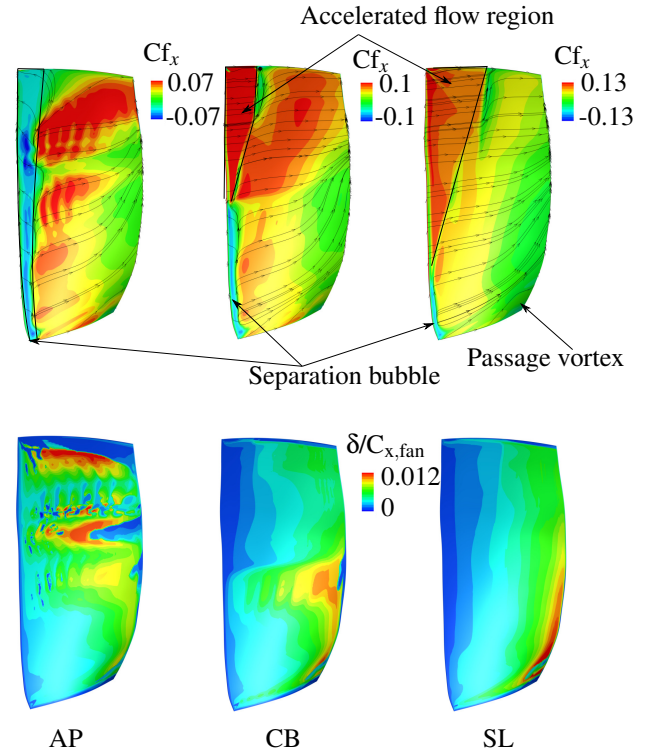


Fig. 13: Axial friction coefficient (top) and boundary layer thickness (bottom) on the fan SS for the different operating points: AP (left), CB (center), SL (right)

the nacelle shown in Fig. 10 where the maximum pressure corresponding to the stagnation point on the rounded front nacelle is shifted with the operating point. Figure 11 shows the axial friction coefficient and streaklines on the hub (spinner) and shroud surfaces. The boundary layer developing from the lip intake on the shroud surface until the fan LE is fully attached. The boundary layer developing on the spinner is also fully attached (see Fig. 11).



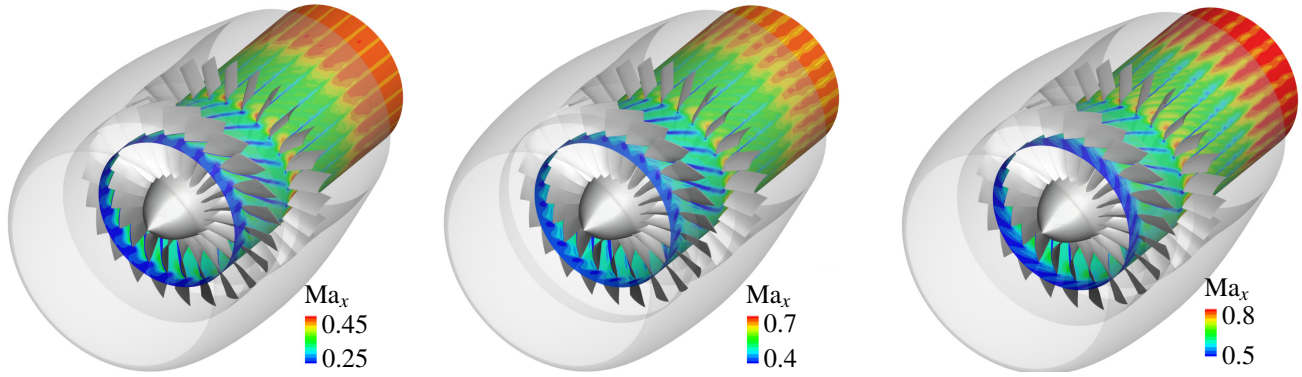


Fig. 14: View of the instantaneous flow colored by the axial Mach number  $Ma_x$  at 50% fan span height for the three operating points: AP (left), CB (center), SL (right) and LC configuration

## 5.2 Flow around the fan blade

Figure 12 shows the radial profiles of total pressure at the beginning of the spinner. The boundary layer thickness at the shroud upstream of the fan in  $\delta/D = 0.02$ . In addition, the axial friction coefficient and boundary layer thickness on the fan Suction Side (SS) for the three different operating points are shown in Fig. 13. At AP, on the fan SS, a localized separation bubble over the full span from the LE to  $x/C_{x, fan} = 10\%$  characterized by negative values of the axial friction coefficient and reversed flow is observed. At a constant mass flow rate, the relatively low rotational speed at AP compared to CB and SL would result in a decrease of incidence and prevent the LE separation bubble on the fan blade. However, since the mass flow rate is reduced at AP (and as a consequence the axial velocity) by more than the rotation speed, the incidence is larger and induces the separation bubble. Figure 14 shows the instantaneous flow topology at mid fan height (axial Mach number) for the different operating points. The vortices released by the separation bubble at AP mixes out with the wake and contribute to a thicker wake compared to SL. The flow on the blade SS migrates radially towards the casing due to the influence of a growing hub secondary flow. Figure 15 shows the relative Mach contours at 80% of the fan height. From 80% span height to the tip, due to the higher rotational speed, a bow shock occurs just upstream of the fan LE. Downstream of the bow shock, due to the sharp curvature of the fan LE, the flow accelerates characterized by high positive axial friction coefficient delaying the formation of the separation bubble (see Fig. 13 middle). Figure 16 shows the pressure coefficient  $C_p = -p/p_\infty$  where  $p$  is the static pressure at the fan blade wall at 90, 50 and 10% of the blade height for the different operating points. The pressure coefficient is nearly constant between the fan LE and the position of the passage shock on the fan blade SS. At SL, a similar topology compared to CB can be observed except that the acceleration of the flow downstream of the shock is of a larger extent and is initialized at around 30% of the blade span height due to the increase of the rotational velocity. The boundary layer thickness is relatively insensitive of the operating point with a boundary thickness at the TE corresponding to around 1.2% of the midspan axial chord

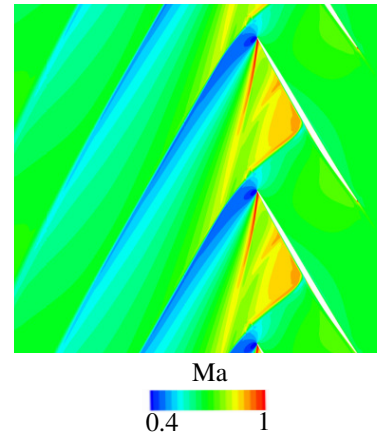


Fig. 15: Mach contours at 80% fan height for the SL operating point

(see Fig. 13 bottom) despite the shock region that marginally delays the boundary layer development.

## 5.3 Flow around the OGV and bypass jet flow

Figure 17 shows an instantaneous view of the OGV SS at AP based on a  $Q$ -criterion  $Q = 10^6$  colored by the normalized streamwise vorticity. The incident flow for the OGV blade is composed of the SS separation vortices at AP, the passage vortex at hub and the tip vortex close to the shroud. Figure 18 shows the SS boundary layer thickness for the three different OGV geometries at CB. On the SS, the flow is essentially two dimensional except close to the hub and shroud where the migration of the passage vortices can be observed. The flow is fully attached at all operating point. Figure 19 shows the pressure coefficient distribution around the LN OGV at 90, 50 and 10% of blade height for the different operating points. The pressure loading on the OGV is almost constant at all span based on the pressure coefficient. The boundary layer thickness at the SS TE is  $\delta/C_{x, OGV} = 0.01$  indifferently of the operating point. Downstream of the OGV, the flow is perfectly axial and the velocity keeps increasing due to the channel contraction until  $Ma_x = 0.45$  at AP,  $Ma_x = 0.65$  at CB and  $Ma_x = 0.75$  at SL (see Fig. 14).

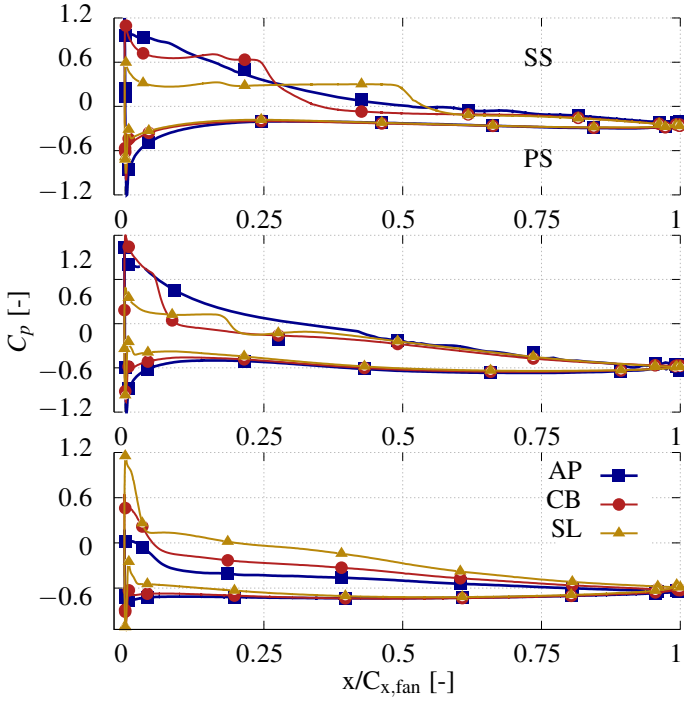


Fig. 16: Pressure coefficient distribution around the fan blade at 90 (top), 50 (middle) and 10% (bottom) of blade height for the different operating points

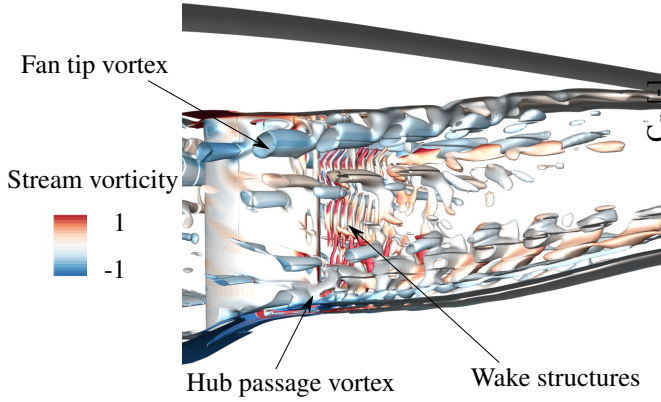


Fig. 17: Instantaneous view of the OGV SS at AP based on a Q-criterion  $Q = 10^6$  colored by the normalized streamwise vorticity

## 6 Loss analysis

The analysis of the losses generated in the configuration is based on the measure of entropy introduced in Sec. 3. Figure 20 shows the two types of plots used to follow the evolution of entropy along the simulation domain: the volume integral of the terms calculated in each grid cell (Eq.(3)) between the inlet and a position  $x$  provides the accumulated entropy  $(s_{\nabla u})_{acc}$  (see Fig. 20 top left); the integration of these same terms over a small axial control volume of axial length  $dx$  around the position  $x$  provides the entropy production  $(s_{\nabla u})_{prod}$  and is used to highlight the areas of strong entropy production, i.e. strong losses (see Fig. 20 top right). In ad-

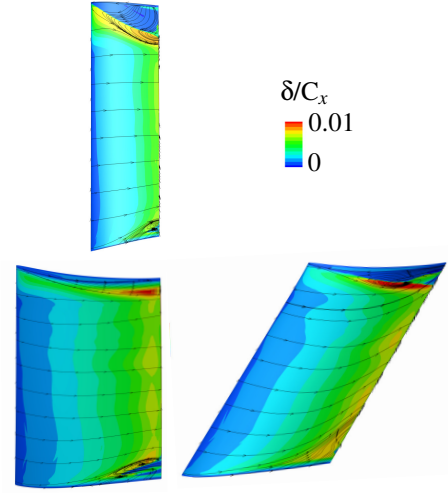


Fig. 18: SS Boundary layer thickness and streaklines for the three different OGV geometries at CB

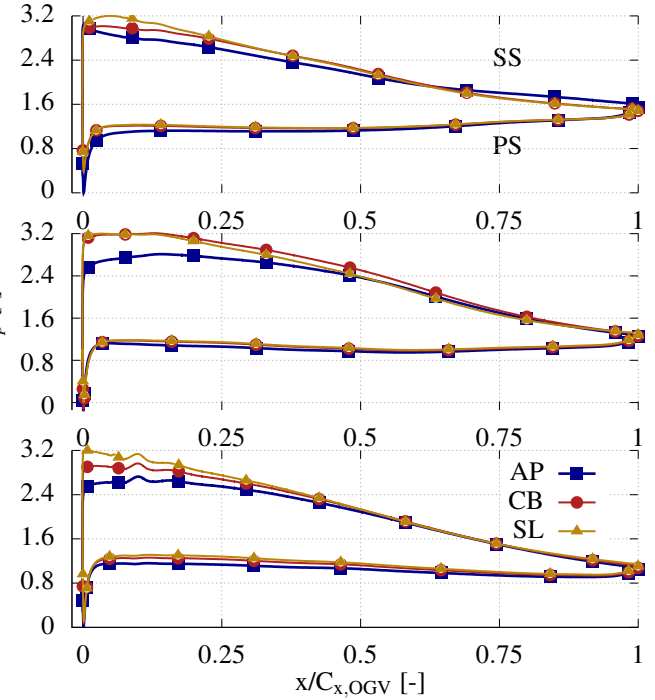


Fig. 19: Pressure coefficient distribution around the LN OGV at 90 (top), 50 (middle) and 10% (bottom) of blade height for the different operating points

dition, to turn the entropy integrated over the considered domain into an entropy loss coefficient, the integrated entropy is divided by the mass flow rate and by a reference dynamic head at the station 1 downstream of the fan for the different operating points based on the mean velocity magnitude over this plane:

$$\zeta(s) = \frac{T \iiint_{\mathcal{V}} s d\mathcal{V}}{\frac{1}{2} \dot{m}_1 (u_{x,1}^2 + u_{r,1}^2 + u_{\theta,1}^2)}. \quad (6)$$

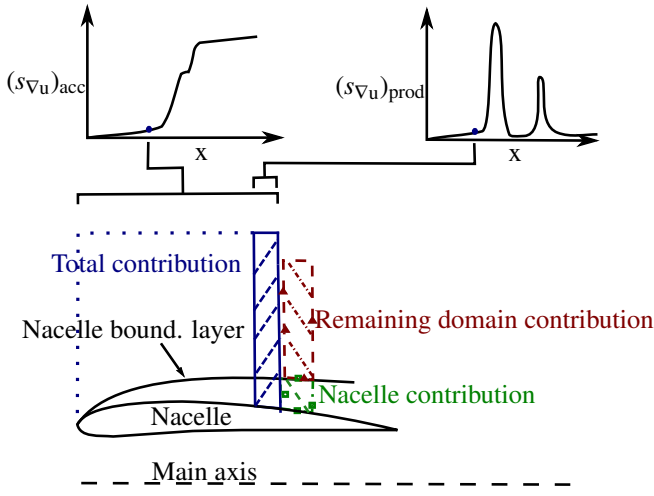
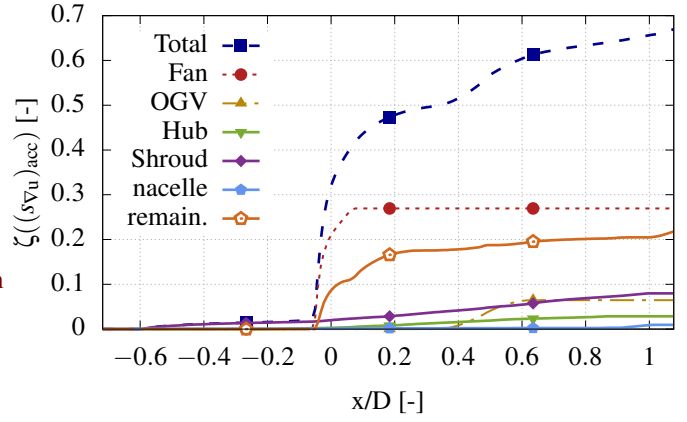
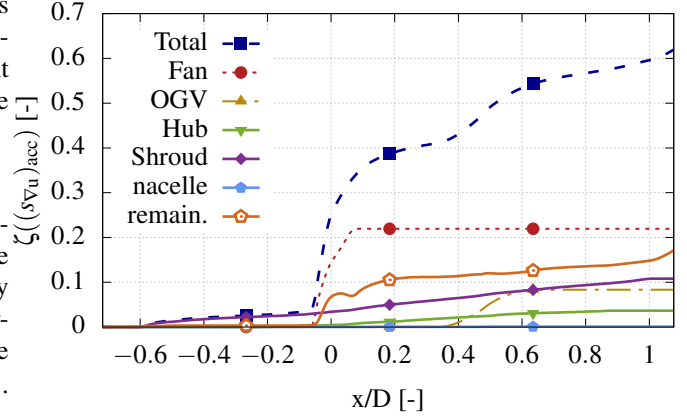


Fig. 20: Simulation domain discretized in axial subvolumes (dark blue). This subvolume can be split into two subvolumes: the nacelle boundary layer (green) and its complement corresponding to the whole subvolume less the subvolume associated with the nacelle boundary layer (red)

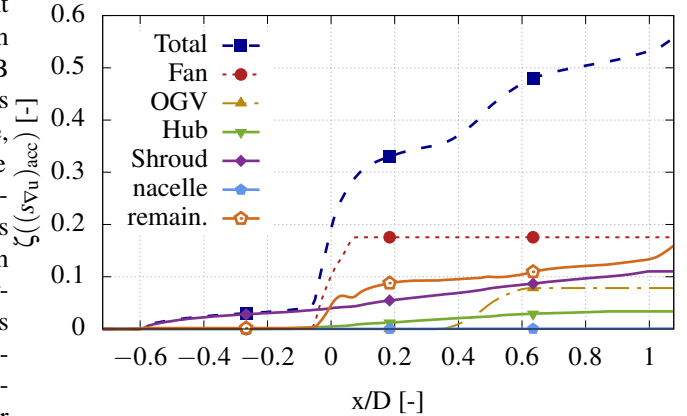
where  $s$  can be the accumulated entropy  $(s_{\nabla u})_{\text{acc}}$  or the entropy production  $(s_{\nabla u})_{\text{prod}}$ . Based on the boundary layer edge detection method introduced in previous Sec. 5, the boundary layer thickness can be obtained for the different wetted surfaces of the domain (hub, shroud, nacelle, fan, OGV) and the corresponding volumes  $\mathcal{V}_{\text{hub}}$ ,  $\mathcal{V}_{\text{shroud}}$ ,  $\mathcal{V}_{\text{nacelle}}$ ,  $\mathcal{V}_{\text{fan}}$ ,  $\mathcal{V}_{\text{OGV}}$ . The full simulation domain less the boundary layer contributions provides the remaining domain with an associated volume  $\mathcal{V}_{\text{rem. term.}}$ . The remaining domain contains different structures generating losses: the fan tip leakage flow, the fan passage vortex close to the hub, the shock structures at CB and SL operating points, the fan wake, the passage vortices for the OGVs close to the hub and shroud, the OGVs wake, the shear layer between the secondary exiting flow and the external flow initiated at the nacelle TE. The entropy is integrated on these restricted domains to obtain the contributions of the different boundary layers and the remaining domain in a similar manner to previous studies of the losses in gas turbines [19, 24–26] (see Fig. 20 bottom). The different figures related to the contributions of the boundary layers and remaining domain are given in conjunction with the total contribution of the domain at the same abscissa to give the reader the magnitude of the contribution to the total one. Similarly to previous Sec. 5, the analysis of the losses is conducted for the LN OGV configuration at the three different operating points (AP, CB and SL) and the influence of OGV geometry on the losses is then described. Figure 21 shows the evolution of entropy along the simulation domain and the different contributions for the AP, CB and SL operating points. The entropy starts to increase at the abscissa of the outer nacelle and shroud ( $x/D = -0.6$ ) and all the losses are associated to the boundary layer developing over these two surfaces. The contribution of the hub starts to increase at the location of the spinner ( $x/D = -0.29$ ). These different boundary layer contributions increase almost linearly along the simulation domain. The region of sharp increase of entropy corresponds



(a)



(b)



(c)

Fig. 21: Loss coefficient corresponding to the entropy accumulated in the simulation domain for the AP (a), CB (b) and SL (c) operating points and LN configuration based on the different contributions

to the fan stage and with a lower magnitude to the OGVs. Similarly to the other wetted surfaces, boundary layers develop around the PS and SS of these two rows and induce a strong increase in entropy at the location of the fan between  $x/D = -0.05$  and  $x/D = 0.07$  and between  $x/D = 0.33$  and  $x/D = 0.48$  for the OGV. When these different contributions

Table 4: Repartition of entropy loss coefficient for the different operating points based on the LN configuration

Contribution	AP	CB	SL
Total	0.675	0.619	0.561
fan	0.271	0.219	0.177
fan SS	0.225	0.160	0.117
fan PS	0.046	0.059	0.060
OGV	0.065	0.083	0.079
OGV SS	0.045	0.058	0.056
OGV PS	0.020	0.025	0.023
Shroud	0.08	0.108	0.111
Hub	0.029	0.036	0.034
Nacelle	0.01	0.005	0.004
Remain. domain	0.219	0.171	0.160
Tip gap	0.052	0.044	0.042

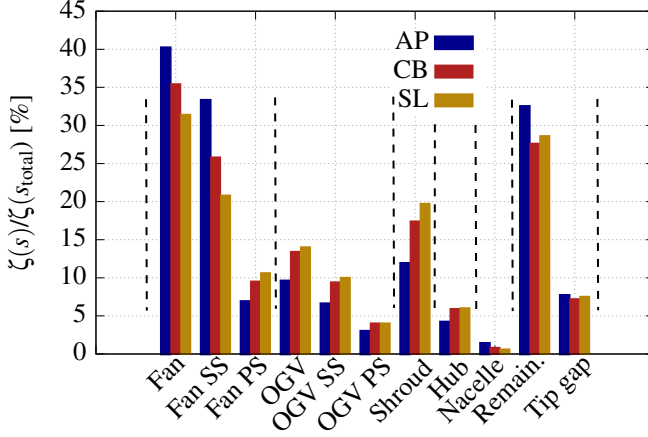


Fig. 22: Repartition of the total losses generated in the NASA SDT configuration based on the different boundary layer contributions and remaining domain (in % of the total losses generated)

are subtracted from the total contribution, the losses referred as remaining domain containing secondary flows, wake and shock losses at CB and SL are isolated. This contribution starts to increase along the fan, in the wake and with a lower magnitude downstream along the OGV.

The different contributions can be integrated over the domain (value at the end of the domain in Fig. 21) to obtain the influence on the total amount of losses. The entropy loss coefficient for the different contributions at the different operating points are gathered in Tab. 4 and the relative contribution to the total losses is shown in Fig. 22. For the AP operating point, the hub boundary layer represents 4.2% of the total losses generated and is less than the shroud boundary contribution (11.9%). This corresponds to the lower extent of the hub surface compared to the shroud with a thinner boundary layer and as a consequence a lower influence on the losses generated. The nacelle boundary layer contributes to 1.4% of the total losses. Despite a similar wetted surface compared to the shroud, the velocity at the edge of

the boundary layer is considerably higher for the shroud (accelerated in-duct flow) compared to the nacelle where the edge velocity is mainly the free stream velocity at  $Ma = 0.1$ . The dominant source of loss is the fan boundary layer with 40.2% and around 80% of the contribution on the SS (33.3% of the total loss) and 20% on the PS (6.9% of the total loss). The flow on the SS diffuses the flow and is therefore subjects the boundary layer to a higher adverse static pressure than the PS. The OGV boundary layer represents 9.6% of the total losses with 2/3 due to the SS and 1/3 to the PS. The remaining domain is a strong contributor to losses with 32.5% of the losses. This contribution starts to increase very close to the fan LE ( $x/D = -0.05$ ) and can be related to the SS separation bubble that generates strong vortices that are dissipated within the inter-blade passage and generates losses. This contribution also increases at the fan TE ( $x/D = 0.07$ ) due to the hub passage vortex, tip vortex and wake structures dissipated in the passage.

At CB and SL, the hub and shroud boundary layer relative contribution to losses increase with 6.0% for the hub and 19.7% for the shroud at SL (compared to 4.2% and 11.9% at AP, respectively). The relative contribution of the nacelle boundary layer decreases with the increasing rotational speed (0.8% of the total losses at CB and 0.6% of losses at SL, respectively) The relative contribution of the fan boundary layer decreases with the increasing rotational velocity, respectively at 35.4% at CB and 31.4% at SL. This decrease of the losses associated to the fan is mainly related to a decrease of the losses generated on the SS. This can be attributed to the attached flow on the fan SS over the upper part of the blade at CB and SL while a localized separation bubble occurred over the full span at AP. The relative contribution of the OGV increases with the rotational speed. The relative contribution of the remaining domain is lower at higher rotational speed with 27.6% at CB and 28.6% at SL compared to the 32.5% of relative contribution to losses at AP. The main difference in the losses related to the remaining domain between the different operating points occurs along the fan blade. At AP, the SS recirculation zone induces vortical structures released in the inter-blade channel, this phenomenon is reduced at CB and SL. At CB, the LE recirculation zone extends from the hub to midspan and at SL from the hub to 30% span height for the SL.

The shock structures induce additional losses in the remaining domain at CB and SL since entropy increases when crossing the shock. In the theoretical formulation, shocks are discontinuity with a corresponding surface of negligible thickness, in the order of magnitude of a mean free path. Numerically speaking, with a finite volume computation, the flow quantity in the simulation domain are continuous. As a consequence, the surface of the shock is indeed enclosing a finite size volume. The corresponding volume is obtained based on a physical shock criterion introduced by Lovely and Haines [27] to determine whether a given cell should be con-



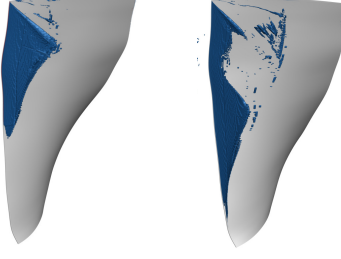


Fig. 23: Tagged cells ( $\Psi \geq 0.95$ ) defining the shock wave volume at CB (left) and SL (right)

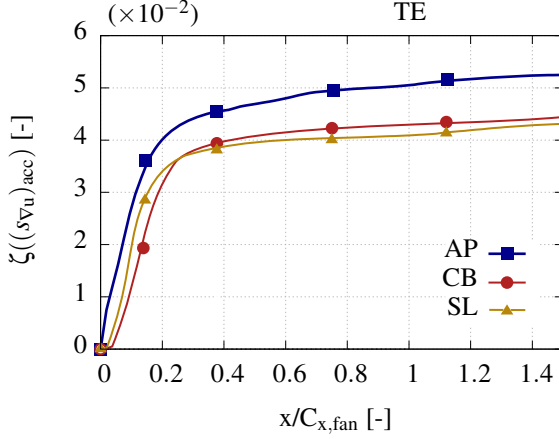


Fig. 24: Loss coefficient corresponding to the entropy accumulated in the tip gap for the AP (a), CB (b) and SL (c) operating points and LN configuration

sidered as being enclosed by the shock surface:

$$\Psi = \frac{u_i \cdot \frac{\partial p}{\partial x_i}}{c(\sum_i |\frac{\partial p}{\partial x_i}|)} \quad (7)$$

where  $c$  is the local speed of sound. If  $\Psi \geq 0.95$  the cell is considered as being enclosed by the wave volume. The corresponding tagged cells for the CB and SL operating points are shown in Fig. 23.

The integration of the entropy on these shock wave volumes represent a contribution of around 1.5% of the remaining domain contribution at CB and 1.8% at SL. This shock wave contribution is relatively low due to an incident Ma marginally higher than 1 (see Fig. 15) inducing a weak gap in the flow quantities and as a consequence in the losses generated.

In order to isolate the losses associated with the tip gap flow above the fan blade, the upper part of the remaining domain has been conserved at a radius between 97% and 100% of the channel height and between the LE of the fan blade and 50% axial fan chord downstream of the fan TE. The radial extent considered is higher than the tip gap corresponding to 0.25% of the channel height but makes possible to account for the tip vortex moving radially in the passage.

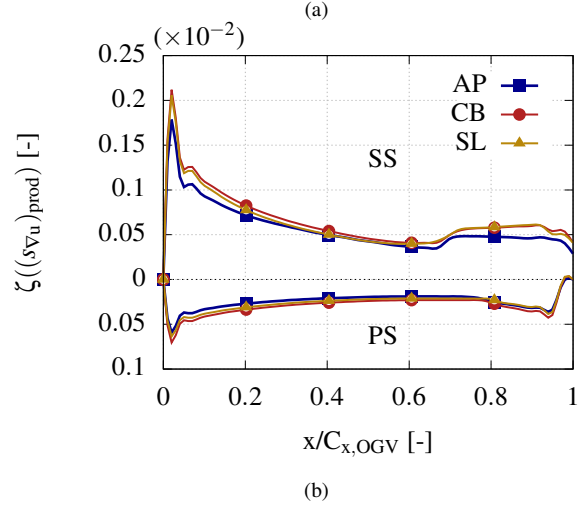
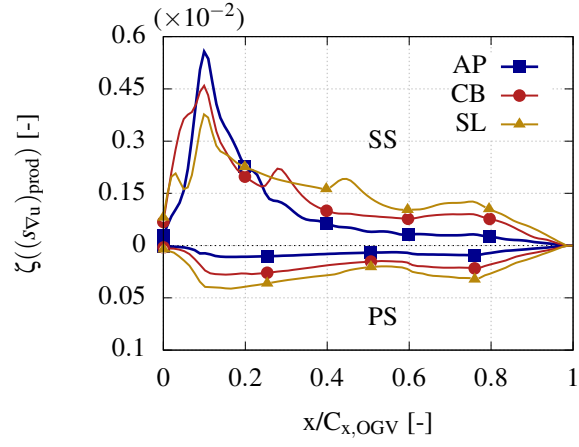


Fig. 25: Entropy production on the fan (a) and LN OGV SS and PS (b) at the different operating points

Figure 24 shows the entropy loss coefficient associated integrated from the fan LE for the different operating points. For the losses associated the tip gap, two main trends can be identified: between  $x/C_{x,fan} = 0$  and  $0.4$ , the losses sharply increases and a second region between  $x/C_{x,fan} = 0.4$  and  $1.5$  where the losses increases less rapidly, but keeps increasing downstream of the TE. The losses associated to the tip gap corresponds to 20-25% of the losses generated in the remaining domain and 7-8% of the total losses generated in the configuration depending on the operating point (see Tab. 4).

The entropy production on the fan SS and PS for the different operating points is shown in Fig. 25a. On the SS, the entropy is mainly produced close to the LE. On this front region, the highest losses are generated at the AP operating point associated to the SS separation bubble. On the rear region of the fan, the losses are higher at a larger rotational speed. On the PS, the losses increase with the rotational speed with a same trend. Figure 25b shows the entropy production on the LN OGV SS and PS at the different operating points. Similarly to the fan blade, the majority of the losses generated on the OGV SS occurs close to the LE. The losses generated increase with the rotational speed. Figure 26 shows the entropy production on the OGV SS and PS

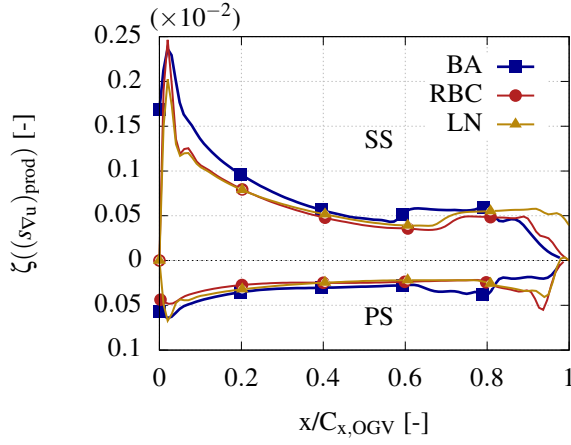


Fig. 26: Entropy production on the OGV SS and PS for the different geometries at CB operating point

for the different geometries at CB. The trend of entropy production for the BA and LC OGV geometries is similar to the LN OGV geometry with the larger increase observed close to the LE. In terms of magnitude, the BA OGV geometries generate more entropy making this geometry more detrimental in the purpose to decrease the losses generated.

## 7 Conclusion

The numerical simulation of the NASA SDT for the three different operating points corresponding to approach, cutback and sideline and the three OGV geometries (baseline, low-count and low-noise) has been performed based on URANS with phase-lagged assumption and POD data storage approach. The simulations showed a good matching with the experimental data: the performance quantities showed a maximum discrepancy of around 1% and 5% for the velocity profiles downstream of the fan.

At approach, the fan is characterized by a leading edge separation bubble over the full span due to a high incidence of the flow generating wide vortices. At cutback and sideline, this recirculation zone is restricted to the lower span heights. On the upper part of the blade, a shock occurs just upstream of the fan leading edge.

The analysis of the losses based on an entropy approach shows that the hub and shroud boundary layers contribute between 10 and 20% to the total loss generated depending on the operating point. The fan boundary layer contributes between 30 and 40% of total losses and between 10 and 15% for the OGVs. On the fan blade, the losses are mainly generated close to the leading edge on the suction side. At approach, larger losses are induced on the suction side compared to the cutback and sideline operating points due to the leading edge separation bubble. The remaining contribution covers around 30% of the losses generated. This includes the fan passage vortex close to the hub, tip fan vortex and passage vortices in the OGV, and the wakes of these two rows. At low rotational speed, the vortical structures released by the fan suction side induce additional losses. At cutback and sideline, the losses associated to the shock waves are weak

since the incident Mach number is only marginally higher than unity.

The breakdown of the losses investigated with URANS could also be used to perform a noise source breakdown and improve the fan design. In this case, the URANS data would be used as an input to a computational aeroacoustics or analytical model that would calculate the acoustic response and so allow a noise source ranking based on the losses split.

## Acknowledgments

The authors wish to acknowledge Edmane Envia from NASA Glenn Research Center for providing the geometry and experimental data of the NASA SDT, Airbus for technical support, the European commission for having funded this research project within the project SCONE (Grant agreement 755543) and to ONERA for licensing Cerfacs to use the code elsA.. Numerical post-processing has been performed using the python-based library Antares. Part of this work was performed using HPC resources from GENCI-[CCRT-CINES-IDRIS] (Grant 2020-[A0062A06074]).

## Nomenclature

Latin letters:

$c$	speed of sound
$C_f$	friction coefficient
$C_x$	axial chord-length
$C_p$	pressure coefficient
$D$	fan diameter
$L$	Length
$Ma$	Mach number $u/c$
$\dot{m}$	mass flow rate
$p$	pressure
$Re_{C_x}$	Reynolds number $u_1 C_x/\nu$
$S$	blade surface
$s$	entropy
$T$	temperature
$t$	time
$u$	velocity
$\mathcal{V}'$	control volume
$(x, y, z)$	cartesian coordinates
$(x, r, \theta)$	cylindrical coordinates

Greek letters:

$\delta$	boundary layer thickness
$\gamma$	heat capacity ratio
$\rho$	density
$\eta$	adiabatic efficiency
$\lambda$	thermal conductivity
$\mu$	dynamic viscosity
$\Omega$	vorticity
$\omega$	rotational speed
$\pi$	compression ratio
$\tau$	viscous stress tensor
$\Psi$	shock wave parameter
$\zeta$	entropy loss coefficient

## Subscripts and superscripts:

mean	mean strain
t	total quantity
turb	turbulent
$\frac{t}{t-t}$	total-to-total
$\frac{+}{+}$	non-dimensional wall-units
$\infty$	free stream quantity
$\overline{\quad}$	Reynolds averaged quantity

## Abbreviations

ADP	Aerodynamic Design Point
AP, CB, SL	APproach, CutBack, SideLine
BA, LC, LN	Base, Low-Count, Low-Noise
FSD	Fourier Series Decomposition
LE/TE	Leading Edge/Trailing Edge
OGV	Outlet Guide Vane
POD	Proper Orthogonal Decomposition
(U)RANS	(Unst.) Reynolds Aver. Navier-Stokes
SS/PS	Suction Side/Pressure Side

## References

- [1] Podboy, G. G., Krupar, M. J., Helland, S. M., and Hughes, C. E., 2002. "Steady and unsteady flow field measurements within a NASA 22 inch fan model". In 40th AIAA Aerospace Sciences Meeting and Exhibit.
- [2] Podboy, G. G., Krupar, M. J., Hughes, C. E., and Woodward, R. P., 2002. "Fan noise source diagnostic test - LDV measured flow field results". In 8th AIAA/CEAS Aeroacoustics Conference and Exhibit.
- [3] Heidelberg, L. J., 2002. "Fan noise source diagnostic test - Tone modal structure results". In 8th AIAA/CEAS Aeroacoustics Conference and Exhibit.
- [4] Shur, M., Strelets, M., Travin, A., Spalart, P., and Suzuki, T., 2018. "Unsteady simulations of a fan/outlet-guide-vane system: Aerodynamics and turbulence". *AIAA Journal*.
- [5] Casalino, D., Hazir, A., and Mann, A., 2017. "Turbofan Broadband Noise Prediction Using the Lattice Boltzmann Method". *AIAA Journal*, **56**(2), pp. 132–143.
- [6] Erdos, J., and Alzner, E., 1977. Computation of unsteady transonic flows through rotating and stationary cascades. 1: Method of analysis. Tech. rep., National Aeronautics and Space Administration.
- [7] Berkooz, G., 2002. "The Proper Orthogonal Decomposition in the Analysis of Turbulent Flows". *Annual Review of Fluid Mechanics*, **25**(1), pp. 539–575.
- [8] Mouret, G., Gourdain, N., and Castillon, L., 2015. "Adaptation of Phase-Lagged Boundary Conditions to Large Eddy Simulation in Turbomachinery Configurations". *Journal of Turbomachinery*, **138**(4), p. 041003.
- [9] Cambier, L., and Veillot, J., 2008. "Status of the elsA software for flow simulation and multi-disciplinary applications". In 46th AIAA Aerospace Sciences Meeting and Exhibit, p. 664.
- [10] Cambier, L., Heib, S., and Plot, S., 2013. "The Onera elsA CFD software: input from research and feedback from industry". *Mechanics & Industry*, **14**(3), pp. 159–174.
- [11] Nishikawa, H., Rad, M., and Roe, P., 2013. "A third-order fluctuation splitting scheme that preserves potential flow". In 15th AIAA Computational Fluid Dynamics Conference.
- [12] Wilcox, D. C., 2008. "Formulation of the k- $\omega$  turbulence model revisited". In AIAA Journal.
- [13] Gourdain, N., 2015. "Prediction of the unsteady turbulent flow in an axial compressor stage. Part 1: Comparison of unsteady RANS and LES with experiments". *Computers and Fluids*.
- [14] Gourdain, N., 2015. "Prediction of the unsteady turbulent flow in an axial compressor stage. Part 2: Analysis of unsteady RANS and LES data". *Computers and Fluids*.
- [15] Marmignon, C., Couaillier, V., and Courbet, B., 2011. "Solution Strategies for Integration of Semi-Discretized Flow Equations in elsA and CEDRE". *AerospaceLab Journal*, **2**(1), pp. 1–11.
- [16] Cliquet, J., Houdeville, R., and Arnal, D., 2008. "Application of Laminar-Turbulent Transition Criteria in Navier-Stokes Computations". *AIAA Journal*, **46**(5), pp. 1182–1190.
- [17] Cousteix, J., 1986. "Three-Dimensional and Unsteady Boundary-Layer Computations". *Annual Review of Fluid Mechanics*, **18**(2), pp. 173–196.
- [18] Michelassi, V., Martelli, F., Dénos, D. J., Arts, T., and Sieverding, C. H., 1999. "Unsteady heat transfer in stator-rotor interaction by two-equation turbulence model". *Journal of Turbomachinery*, **121**(3), pp. 436–447.
- [19] Denton, J. D., 1993. "Loss Mechanisms in Turbomachines". *Journal of Turbomachinery*, **115**(4), p. 621.
- [20] Lengani, D., Simoni, D., Ubaldi, M., Zunino, P., Bertini, F., and Michelassi, V., 2017. "Accurate Estimation of Profile Losses and Analysis of Loss Generation Mechanisms in a Turbine Cascade". *Journal of Turbomachinery*, **139**(12), pp. 121–132.
- [21] Moore, J., and Moore, J. G., 1983. "Entropy Production Rates From Viscous Flow Calculations: Part I - A Turbulent Boundary Layer Flow". In Volume 1: Turbomachinery, ASME, p. V001T01A032.
- [22] Hughes, C. E., Jeracki, R. J., Woodward, R. P., and Miller, C. J., 2002. "Fan noise source diagnostic test - Rotor alone aerodynamic performance results". In 8th AIAA/CEAS Aeroacoustics Conference and Exhibit.
- [23] Smith, B. R., 1995. "Prediction of hypersonic shock wave turbulent boundary layer interactions with the k-l two equation turbulence model". In 33rd Aerospace Sciences Meeting and Exhibit.
- [24] Denton, J. D., and Pullan, G., 2012. "A Numerical Investigation Into the Sources of Endwall Loss in Axial Flow Turbines". In Volume 8: Turbomachinery, Parts A, B, and C, p. 1417.
- [25] Hammer, F., Sandham, N., and Sandberg, R., 2018. "The Influence of Different Wake Profiles on Losses in a Low Pressure Turbine Cascade". *International Journal of Turbomachinery, Propulsion and Power*.
- [26] Lengani, D., Simoni, D., Pichler, R., Sandberg, R. D., Michelassi, V., and Bertini, F., 2018. "Identification and quantification of losses in a LPT cascade by POD applied to LES data". *International Journal of Heat and Fluid Flow*, **70**, pp. 28–40.
- [27] Lovely, D., and Haimes, R., 1999. "Shock detection from computational fluid dynamics results". In 14th Computational Fluid Dynamics Conference.